

# Influence of liquid environment on the properties of laser ablation produced tungsten nanostructures

Zohreh Famili, , Davoud Dorrnian\* , Amir Hossein Sari

## Abstract

Impacts of the liquid environment on the characteristics of pulsed laser ablation (PLA) in liquid synthesized tungsten (W) nanostructures have been investigated. High purity W target was irradiated by the fundamental harmonic of a Q-switched Nd: YAG laser of 7 ns pulse width and 1 J/cm<sup>2</sup> laser fluence in different liquid environments including distilled water, ethanol, acetone, and cetrimonium bromide (CTAB) solutions. Structural, chemical, and optical properties of W nanoparticles (NPs) were characterized by field emission scanning electron microscopy, transmission electron microscopy, X-ray diffraction, photoluminescence, FTIR, and UV-Vis-NIR absorption spectroscopy techniques. FTIR spectra indicate the formation of a bond between W and O in the synthesized NPs, and XRD patterns confirm producing W and WO<sub>3</sub> composite NPs in all liquid environments. The excitonic/plasmonic absorption peak of W/WO<sub>3</sub> NPs occurred in the absorption spectra of all samples. The largest particles with the lowest adhesion were synthesized in acetone solution and adding CTAB surfactant to distilled water reduced the adhesion of NPs. The PL spectra present band-to-band transitions and oxygen vacancies of WO<sub>3</sub>.

## Keywords

W-WO<sub>3</sub> composite nanoparticles; Liquid environment; Laser ablation; Exciton; Surface plasmon; Core-shell.

Laser lab., Plasma Physics Research Center, Science and Research Branch, Islamic Azad University, Tehran, Iran

\*Corresponding author: doran@srbiau.ac.ir

## 1. Introduction

Recently, nanostructures have been utilized in widespread domains of sciences and technology. Among them, W and its oxide nanostructures have unique electrical, gasochromic, and photoelectrochromic properties so that can be used in infrared switching devices, photovoltaic organic solar cells, photocatalysis, gas and chemical sensors, biosensors, supercapacitors, information storage media, optical modulators, and the like [1–4].

The PLA of metal targets in liquid is known as a facile, fast, green, and cheap method for producing not only pure metal nanostructures but also metal oxides, carbides, and alloys. In addition, in this method, there are many parameters concerning the source and the liquid environment for controlling the size, shape, and composition of the products [5–7]. Numerous studies have shown that the properties of NPs produced by PLA of a metal target in liquid environments strongly depend on the characteristics of the target material, the liquid environment, and the laser beam [8–10].

In this work, the PLA of W target in several liquids is performed, then the effect of these liquids on the properties of products such as size, shape, and composition has been studied. Liquid environments used in the ablation process were distilled water and ethanol, acetone, and CTAB aqueous solutions. The choice of these liquids is due to their different properties such as chemical composition, density, viscosity,

polarity, and so on.

Water (H<sub>2</sub>O) and ethanol (CH<sub>3</sub>-CH<sub>2</sub>-OH) are polar protic solvents, and there is a hydrogen bond between molecules in water and ethanol due to the presence of the OH functional group. Of course, the hydrogen bond between ethanol molecules is weaker than in water. The hydrogen bond causes exclusive properties such as high specific heat capacity, latent heat of vaporization, and surface tension in the solvent. In addition to creating attraction between solvent molecules, the hydrogen bond is responsible for the attraction between solvent molecules and other molecules or surfaces. Acetone (CH<sub>3</sub>-CO-CH<sub>3</sub>) is an aprotic polar solvent whose forces between its molecules are dipole-dipole. The dipole moment of ethanol, water, and acetone are 1.69 D, 1.85 D, and 2.88 D, respectively. To be stronger dipole moment of acetone is due to the presence of a double bond of oxygen to carbon in its carbonyl group C=O [4, 11–13].

Adding surfactant to ablation liquid has a significant effect on the size, adhesion, and composition of NPs produced by PLA in a liquid environment. Surfactants are organic compounds containing two parts, a non-polar part which consists of a long hydrocarbon chain (hydrophobic tail), and a polar part which is generally ionic (hydrophilic head). Surfactants are soluble in both water and organic solvents due to their dual nature. One part of the surfactants is soluble, and the other part is insoluble. The molecules of surfactants preferentially orient so that the soluble part bonds to the liquid and the insoluble to

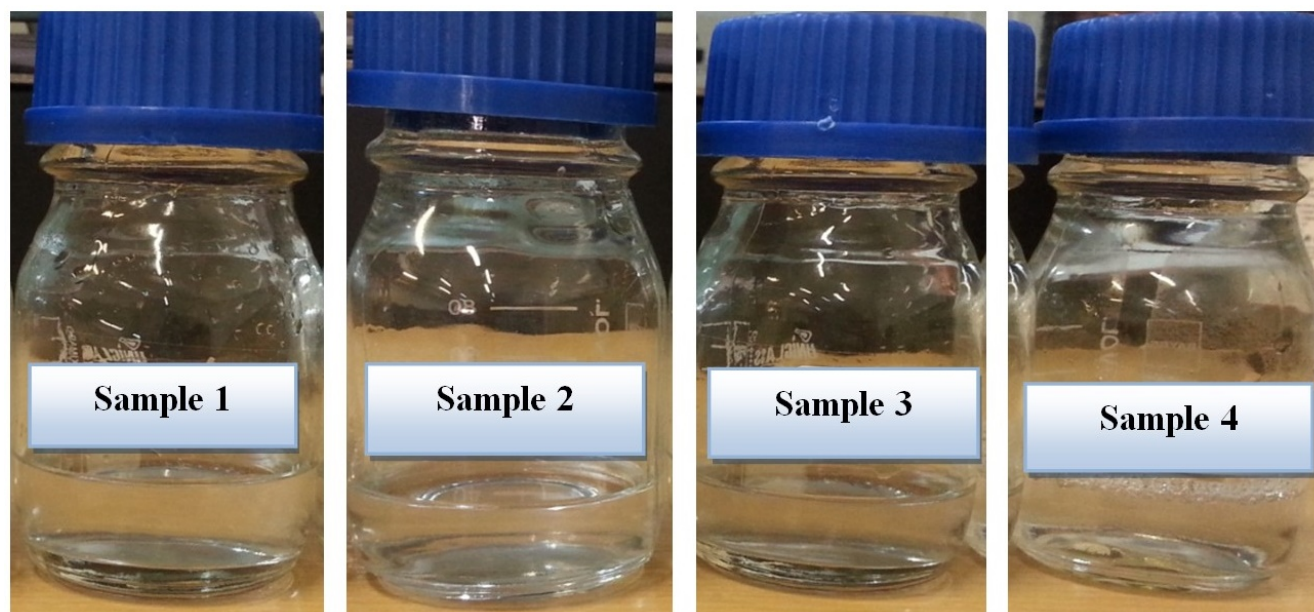


**Figure 1.** Colloidal samples prepared by PLA of W target in different liquid environments.

the solid surface. These materials change the surface energy and tend to accumulate at the interface between the two environments. CTAB with the chemical formula  $C_{19}H_{42}BrN$  is a cationic surfactant with a positively charged ionic hydrophilic head and a non-polar hydrophobic tail [14–16].

In the PLA of a target in a liquid environment, some properties of liquid such as density, viscosity, thermal conductivity, specific heat capacity, etc, control the size, and morphology of the products by affecting the evolution, expansion, temperature reduction, and collapse time of plasma plume and cavitation bubbles. Other properties of the liquid, such as its nature of polarity and dispersion affect the adhesion and aggregation of NPs [2, 6, 16–18]. Therefore, some effective physical and chemical properties of materials used in PLA of the W target in a liquid environment are given in Table 1. The data in the table are taken from references [19–21]. Of course, in ethanol/acetone solution, these parameters are affected by the ratio of ethanol/acetone to water. Also, the mentioned parameters change in aqueous CTAB solution compared to distilled water with due attention to the molarity of the solution. We have used the data in this table to discuss the results of various analyses.

## 2. Experimental setup

The synthesis of colloidal NPs is performed by the PLA of a W plate (99.9%) with 2 mm thickness in distilled water, ethanol and acetone diluted with distilled water (ethanol/acetone: water in a 2:1 ratio), and aqueous CTAB solution with the concentration of 0.0027M. Just before the experiment, in order to remove organic compounds, the W plate and the containers were rinsed with ethanol, acetone, and distilled water using an ultrasonic cleaner. The cleaned plate was located at the bot-

tom of a glass vessel containing 30 cc of each ablation liquid environment. The height of the liquid above the surface of the W plate was approximately 8mm. The W target was irradiated vertically with the first harmonic (1064 nm) of a Q-switched Nd: YAG laser operating at a 5 Hz repetition rate with a pulse width of 7 ns. A lens with a focal length of 80 cm is used to focus the laser beam on the W target immersed under the liquid. The W target in each of the mentioned liquids was irradiated with 3000 laser pulses at a  $1.0 \text{ J/cm}^2$  laser fluence before the lens. During laser irradiation, the vessel containing liquid and target was moved manually in different directions on the horizontal surface to ensure uniform ablation and prevent a texturing effect. Colloidal samples prepared by PLA of a W plate in distilled water, ethanol, acetone, and CTAB solutions were named samples 1, 2, 3, and 4, respectively.

The various analytical techniques were utilized for the characterization of the nanostructures prepared in different liquids. Morphological studies and elemental identification were performed using a field emission scanning electron microscope (FESEM; TESCAN MIRA3) coupled with energy dispersive spectrometry (EDS). The size distribution of products was studied using a transmission electron microscope (TEM, Zeiss-EM10C-100 kV). The Fourier transform infrared (FTIR) spectroscopy was performed using Perkin-Elmer FTIR spectrometer (Spectrum Two) in the spectral range of  $450\text{--}4000 \text{ cm}^{-1}$ . In order to study the structural properties of the products, the X-ray diffraction (XRD) patterns were taken of colloidal solutions dried on silicon substrates using PANalytical-X'Pert PRO X-ray diffractometer with Cu  $K\alpha$  source ( $\lambda = 0.1514060 \text{ nm}$ ). The optical properties of colloidal suspensions were evaluated by a UV-vis-NIR spectrometer (PerkinElmer Lambda 950) at room temperature in the range  $200\text{--}1100 \text{ nm}$ . The photoluminescence (PL) spectra of the samples were obtained

using a Fluorescence Spectrophotometer F-4500.

### 3. Results and discussion

#### 3.1 Color of colloidal samples

Figure 1 shows the image of prepared colloidal samples. The composition of NPs and the ablation environment, and the amount and the size of NPs can be factors affecting the color of samples [3]. According to the values obtained for the size of NPs in the following sections, no clear relationship was found between the color of the suspensions and the size of NPs. The discrepancy in the color of the samples may be related to the chemical composition of the ablation environments. The color of sample 1 is light gray. According to the results of the XRD and FTIR analyses, this sample contains W NPs and  $WO_3$  in distilled water, which in other reports for it, depending on the size of NPs, a light gray to dark color was observed [22, 23]. The colors of the colloidal samples 2 and 3 were light gray and light orangish gray respectively. Samples 2 and 3 were darker than sample 1 due to the appearance of carbon in them. Carbon atoms may be released from ethanol and acetone molecules at high plasma temperatures due to high laser fluence [4, 5, 24]. Colloidal sample 4 is colorless, which is expected due to being colorlessness of the suspension of CTAB powder in water.

#### 3.2 EDS analysis

The EDS analysis was performed to investigate the elemental composition of the samples. Figure 2 shows the EDS spectra of samples prepared in different liquid environments. The existence of W and O elements is evident in the spectra of all the samples. The Au signals observed in the EDS spectra are related to the gold coating on samples before EDS analysis [25]. Other elements observed in the spectra are related to the molecules of the liquids used.

#### 3.3 XRD spectra

XRD spectra of NPs prepared by PLA of W target in different liquid environments are shown in Figure 3. In order to perform this measurement, a few drops of each of the colloidal samples were dried on silicon wafer substrates of  $10\text{mm} \times 10\text{mm}$  at room temperature. In the XRD spectra, the broad peak observed at about  $69^\circ$  is attributed to the silicon substrate. According to the PDF card of 01-088-2339, the peaks observed at  $38.37^\circ$ ,  $44.60^\circ$ , and  $77.99^\circ$  corresponding to (111), (200), and (311) Bragg planes, respectively, confirm the formation of the cubic crystal structure of W with Fm-2m(225) space group and lattice parameter as  $a=4.060\text{\AA}$ . The identified structure, which indicates the formation of W metal NPs, has peaks different from the W metal target peaks. W target peaks are observed at  $40.26^\circ$ ,  $58.28^\circ$ ,  $73.20^\circ$ , and  $87.02^\circ$  assigned to (110), (200), (211) and (220) Bragg planes of cubic W with Im-3m(229) space group, and the lattice parameter as  $a=3.165\text{\AA}$  (PDF: 00-004-0806). That means the ablation process of the W target has led to the formation of W metal NPs with

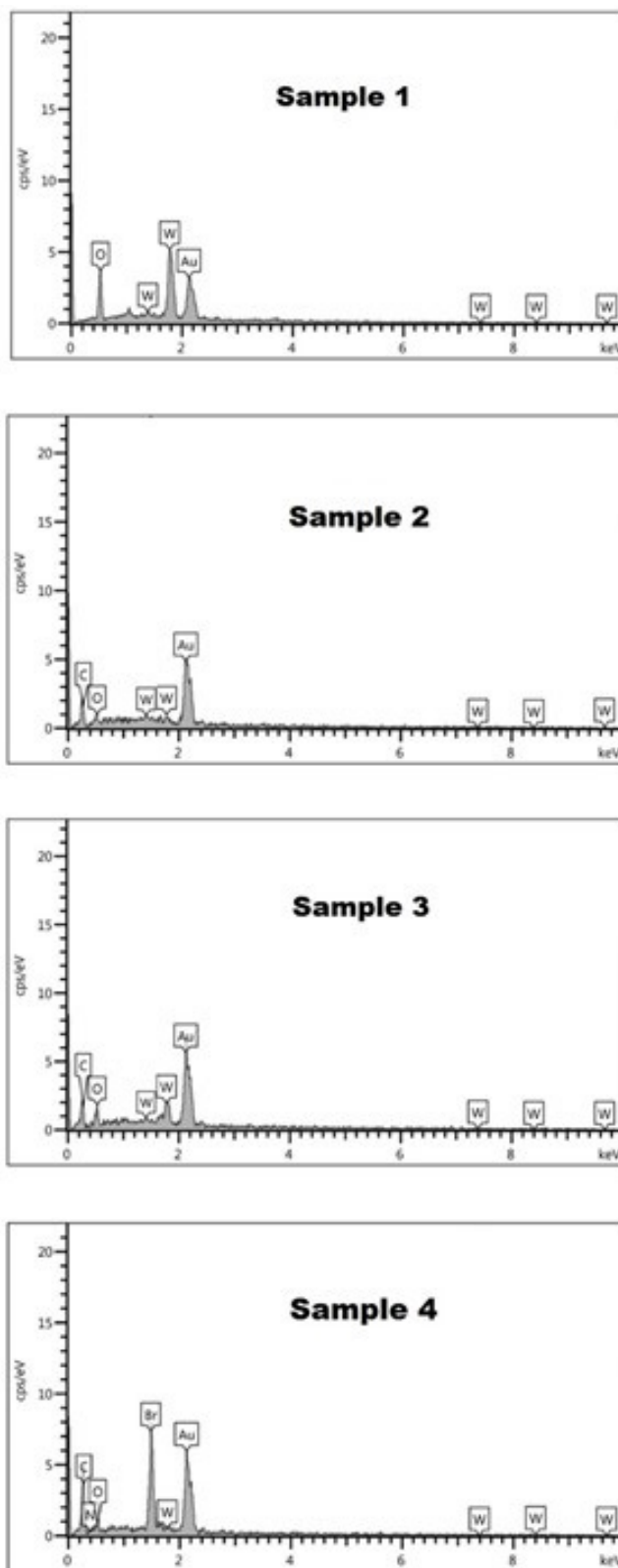


**Figure 2.** EDS spectra of samples prepared in different liquid environments.

different lattice parameters from the W target. According to studies of Zheng and et al, tungsten atoms can have various structures [3]. On the other hand, after ablation of the tungsten target and nucleation during the plasma plume expansion phase, tungsten atoms in a new rearrangement create a crystalline structure with a different lattice constant. The intensity of these peaks in samples 1 and 4 is higher than other samples, which can indicate a higher degree of crystallinity in these samples. Also, in samples 3 and 4, the peak appeared at  $40.26^\circ$  matches with one of the peaks related to the cubic structure of the W target (PDF: 00-004-0806). In the sample 4, the peaks observed at  $17.04^\circ$ ,  $20.64^\circ$ ,  $24.03^\circ$ , and  $27.86^\circ$  corresponding to the Bragg planes (1 0 3), (0 0 12), (0 0 14), and (0 0 16), respectively, are related to the crystal structure of CTAB( $C_{19}H_{42}BrN$ ) (PDF: 00-034-1556).

According to PDF card of 2008-033-1387, the XRD peaks at  $13.96^\circ$ ,  $24.33^\circ$ ,  $44.37^\circ$ , and  $77.70^\circ$ , indexed to (100), (110),

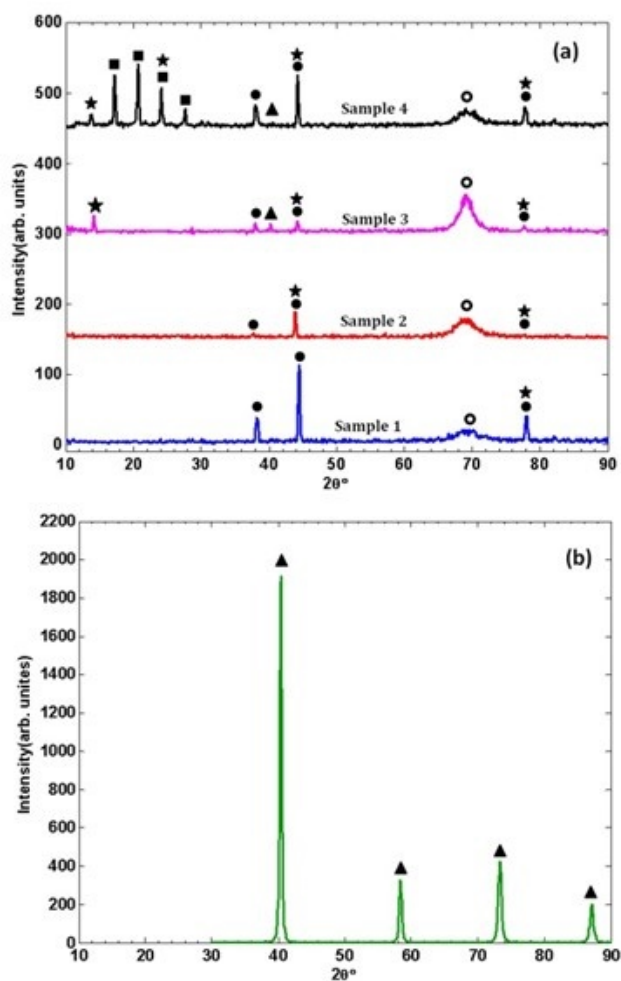


**Figure 3.** XRD spectra of a) samples prepared in different liquid environments and b) W target used in PLA.  $\circ$ : broad peak attributed to the silicon substrate,  $\star$ : Hexagonal  $WO_3$ ,  $\blacksquare$ : CTAB( $C_{19}H_{42}BrN$ )  $\bullet$ : cubic W with Fm-2m(225) space group,  $\blacktriangle$ : cubic W with Im-3m(229) space group

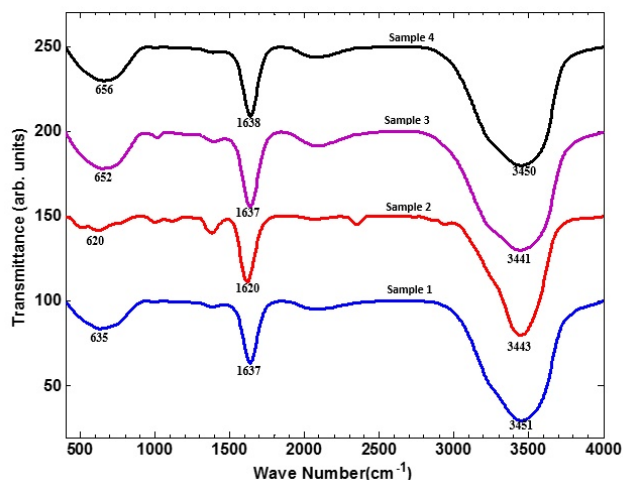


**Figure 4.** FTIR spectra of samples prepared in different liquid environments.

(211), and (402) Bragg planes can be ascribed to the formation of the  $WO_3$  hexagonal phase in the samples [26]. The formation of the  $WO_3$  structure in sample 4 is more significant than other samples, because, in the diffraction pattern of this sample, the number of peaks identifying this structure is more. The peaks of the hexagonal  $WO_3$  structure in sample 3 are weaker, which could be due to the higher dipole moment of acetone compared to ethanol and water. Other reports indicate that the degree of crystallinity of  $WO_3$  NPs in polar liquids is lower than in dispersant liquids [27, 28]. Since the peaks identifying the hexagonal  $WO_3$  structure overlap with the peaks attributed to W and CTAB crystal structures, FTIR analysis was utilized to ensure the formation of  $WO_3$  nanostructure in the samples.

### 3.4 FTIR spectra

The FTIR spectra were taken in the spectral range of  $400\text{--}4000\text{ cm}^{-1}$ . The FTIR spectra of samples prepared by PLA of W target in different environments are shown in Figure 4. The strong and broad absorption peaks in the range of  $3000\text{--}3600\text{ cm}^{-1}$  are ascribed to the stretching modes of OH groups. The medium and broad peaks in the range of  $1620\text{--}1660\text{ cm}^{-1}$  and low-intensity peaks located at about  $1385\text{ cm}^{-1}$  are due to bending modes of water molecules [29, 30]. The bands in the region  $600\text{--}780\text{ cm}^{-1}$  correspond to the stretching modes of bridging oxygen,  $\nu(O\text{--}W\text{--}O)$ , which confirm the formation of  $WO_3$  NPs in different environments [31, 32]. The difference in peak positions of the stretching mode of  $\nu(O\text{--}W\text{--}O)$  in different samples is ascribed to the lengthening of some bonds due to oxygen vacancies or defects in the  $WO_3$  structure. It seems that the characteristic absorption peak of vibration mode of  $\nu(O\text{--}W\text{--}O)$  in NPs produced in other liquid environments than the distilled water environment shifts to a longer wavelength [33, 34].

In summary, the XRD and FTIR spectra clearly show the formation of W and  $WO_3$  NPs in all samples. It seems the

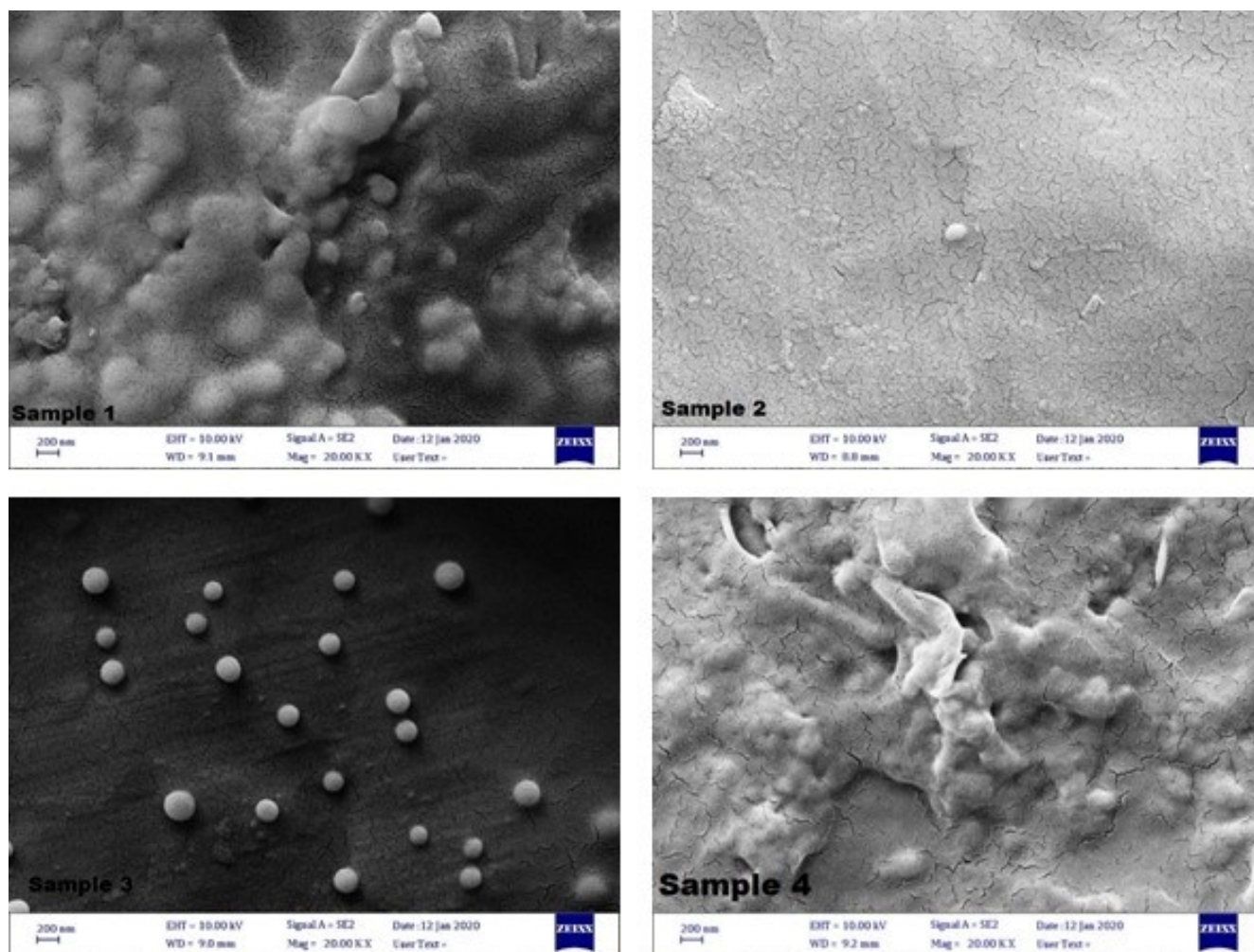


**Figure 5.** FESEM images of W-WO<sub>3</sub> composite NPs prepared in different liquid environments.

metal W NPs have formed during the cooling of the plasma plume. After the collapse of the plasma plume and the dispersion of NPs in the liquid environment, chemical and physical interactions between the ablated W NPs and water molecules in used aqueous environments have formed a surface layer of WO<sub>3</sub> on the metal W NPs.

Investigation of reports on the PLA of W target in aqueous liquid environments shows that different products have been produced depending on the conditions of the PLA process, especially applied laser fluence. In some studies, the production of WO<sub>3</sub> NPs with different phases and compounds has been reported [11]. The production of W metal NPs has been confirmed in several reports [4]. Some studies also suggest the formation of W-WO<sub>3</sub> composite NPs with a structure of core-shell [18, 35]. The formation of W-WO<sub>3</sub> composite NPs can describe in three steps. In the first step, after the interaction between the laser pulse and the W target in the solid-liquid interface, W plasma is rapidly produced with high temperature and high pressure without liquid. In the second step, ultrasonic and adiabatic expansion of W plasma in cavitation bubbles leads to cooling the W plasma plume region

and hence the formation of W NPs. In our work, since the pulse repetition rate and the pulse width were 5 Hz and 7 ns, respectively, the distance between two sequential pulses is 0.2s, which is much longer than the lifetime of a plasma plume. Therefore, the next laser pulse has no interaction with the previous plasma plume. In the third step, after extinguishing the plasma, the W NPs formed are encountered to liquid and surfactant (if any) molecules resulting in some chemical reactions and coating effects of surfactant [28, 36–39].

### 3.5 FESEM and TEM images

The morphology and size distribution of produced NPs were investigated by FESEM and TEM analyses. FESEM images of samples prepared by PLA of a W target in different liquids are shown in Figure 5. The observed results in FESEM images are the formation of strongly adhesive NPs in sample 1, formation of a plate structure in sample 2, formation of non-adhesive NPs in sample 3, and formation of adhesive NPs with a wrinkle in sample 4.

TEM images of NPs prepared by PLA of W target in different liquid environments are presented in Figure 6. TEM images

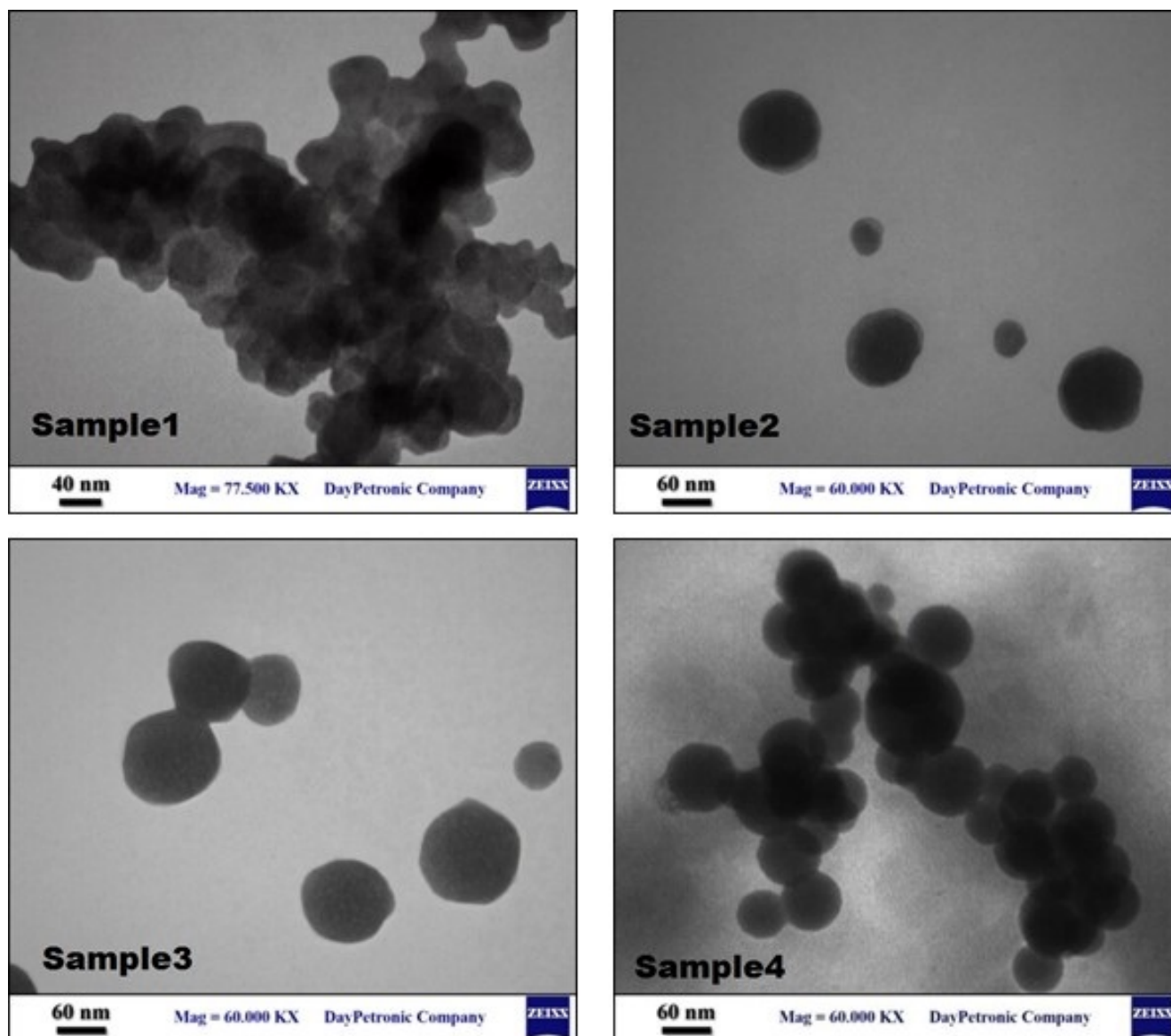


**Figure 6.** TEM images of W-WO<sub>3</sub> composite NPs prepared in different liquid environments.

show the formation of spherical NPs in samples 2-4 and nearly spherical NPs in sample 1. Also, the aggregation of NPs in the distilled water environment is more than in the other environments, and in the acetone aqueous solution is the lowest. Size distribution histograms of NPs are shown in Figure 7. The average size of NPs in samples 1-4 are 49.54, 66.27, 79.24, and 71.01 nm, respectively. In addition, the standard deviation size of the NPs in samples 1-4 are 27.19, 26.67, 32.39, and 35.52 nm, respectively (Figure 7, Table 2). According to these results, NPs have the largest average size and standard deviation in acetone solution. In PLA of a specific target with particular laser parameters in different liquid environments, the differences in the characteristics of the products are related to the properties of used liquids. In the following, the reasons for the observed discrepancy in the morphology,

size, and size distribution of NPs prepared in the various liquid environments are discussed.

The surface charge of metal oxide NPs is different in various liquid environments. Depending on whether the pH of the liquid is greater than or equal to or less than the isoelectric point of NPs, the surface charge of NPs will be negative, zero, and positive, respectively. The surface charge of WO<sub>3</sub> NPs in the various liquids used in our experiment is negative because according to Table 1, the pH of these solutions (about 6.0-7.33) is higher than the isoelectric point of WO<sub>3</sub> (about 0.2-0.5) [40]. As mentioned in Section 1, the dipole moment of acetone molecules is higher than water and ethanol (Table 1). In sample 3, due to the high dipole moment of the acetone molecules, at the interface between the WO<sub>3</sub> NPs and the surrounding liquid, strongly electrical double layers

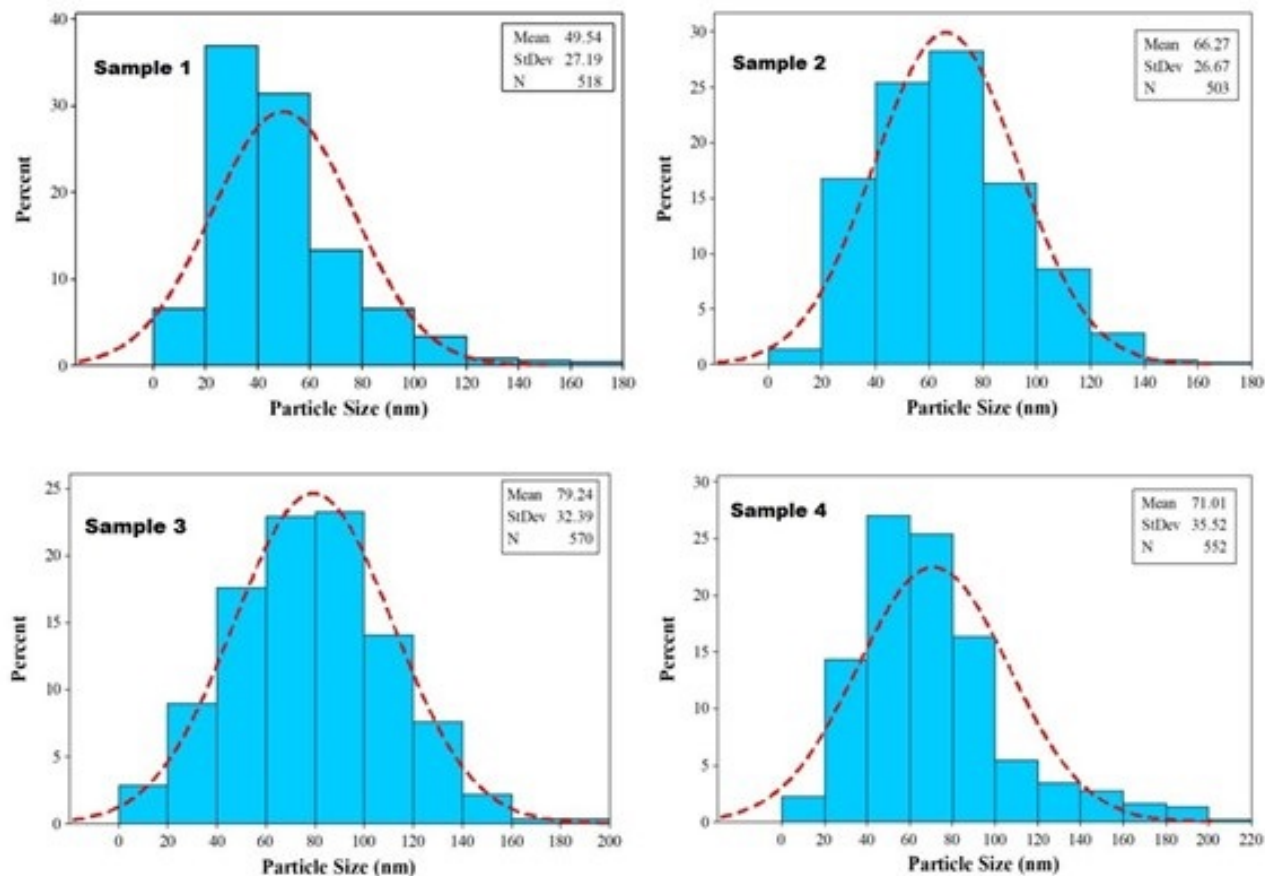


**Figure 7.** Size distribution of W-WO<sub>3</sub> composite NPs prepared in different liquid environments. Data taken from TEM images

are formed, causing the effectively electrical repulsion forces between the WO<sub>3</sub> NPs. Hence, the aggregation and adhesion of NPs produced in acetone solution are smaller than other liquids (see picture 6). On the other hand, in samples 1 and 2, the repulsion between NPs due to the formation of charged double layers competes with the attraction due to hydrogen bonds between NPs and water/ethanol molecules [2,6]. In distilled water environment, the attraction forces due to hydrogen bonds overcome the repulsion forces due to the formation of charged double layers, creating an intense adhesion between NPs (see picture 6).

In our experiment in the aqueous CTAB solution, micelle layers are formed around the NPs because the concentration of CTAB surfactant in this environment is 0.0027 M, which is higher than the critical micelle concentration (CMC) of CTAB (CMC= 0.0009 M for CTAB). The negatively charged surface of WO<sub>3</sub> NPs absorbs the positive head of the CTAB, and the hydrocarbon tail of the CTAB forms a protective micelle layer around the NPs (picture 8). This protective surface reduces the adhesion of NPs in the aqueous CTAB solution relative to distilled water (see picture 6) [16-18].

In the PLA process of a target in a liquid environment, the formation of a larger plasma plume leads to the formation of

larger NPs. Also, the slower the cooling rate of the plasma plume, the larger NPs are produced [41]. Numerous factors such as refractive index, density, viscosity, surface tension, specific heat capacity, and thermal conductivity play a role in the formation and cooling rate of the plasma plume [5,16-21]. First, we investigate the causes of the formation of NPs with different average sizes and size distributions in distilled water, ethanol and acetone solutions. The laser beam reflects twice before reaching the target surface. The first reflection is from the air-liquid interface, and the second is from the liquid-target interface. In a vertical incidence, the reflectance ( $R$ ) of the interface of two environments was calculated using the Fresnel equation following [39]

$$R = \left| \frac{(N_2 - N_1)}{(N_2 + N_1)} \right|^2 \quad (1)$$

where  $N_1$  and  $N_2$  are the complex refractive indexes of the two environments (air and liquid in air-liquid interface or liquid and target in the liquid-target interface). As is seen in Table 1, the refractive index of the used liquids in the PLA process is almost the same. Therefore, the percentage of laser beam energy reflected from the air-liquid /liquid-target interface in the used different liquid environments is approximately equal.

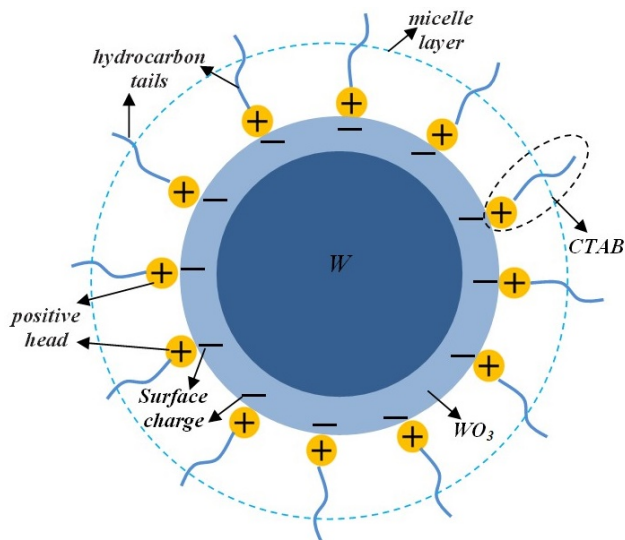


**Figure 8.** Formation of micelle layer around W-WO<sub>3</sub> composite NPs with core-shell structure.

Because, according to Equation (1), what can cause a difference between the reflectance of the interfaces in the different liquids is the difference in the refractive indexes of these liquids, whereas, those are approximately equal (Table 1). The similar light reflectance from the air-liquid/liquid-target interface leads to similar ablation rates in the different liquids used. Therefore, the reflectance of the air-liquid/liquid-target interface can not have a perceptible effect on the difference in the amount of energy received by the target surface in different environments.

However, according to Table 1, at the wavelength used in the ablation process (1064 nm), acetone and ethanol have the same transmittance ~ 1, while pure water has a transmittance of 0.54559. Therefore, in the ablation process in ethanol and

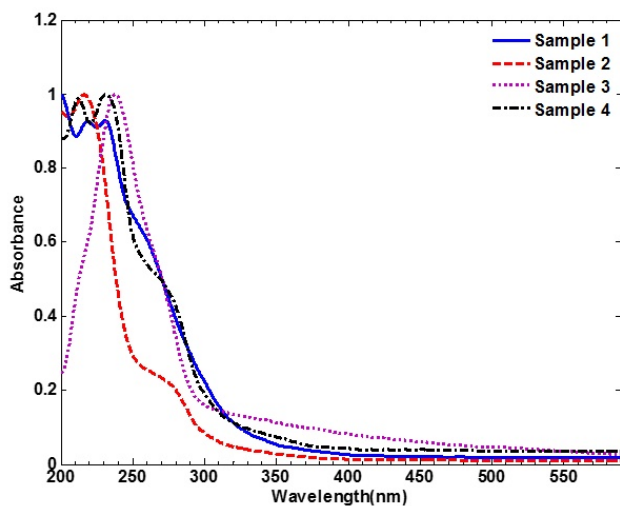


**Figure 9.** UV-vis spectra of W-WO<sub>3</sub> composite NPs prepared in different liquid environments.

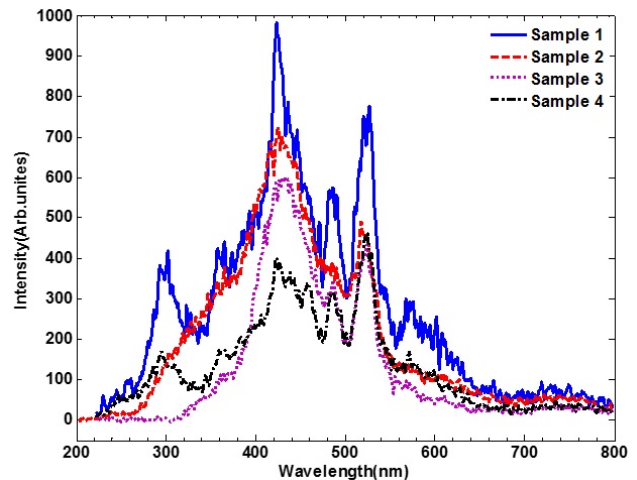


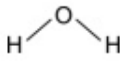
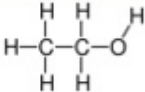
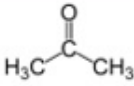
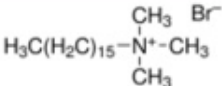
**Figure 10.** PL emission spectra of W-WO<sub>3</sub> composite NPs prepared in different liquid environments at 200 nm excitation wavelength.

acetone solutions, which have higher transmittances than pure water, more laser energy reaches the target surface and causes more material to be ablated from the target surface. The greater the amount of ablated material, the larger the plasma plume, resulting in larger NPs are produced [11,39]. Plasma cooling rate and subsequent condensation also affect the size of colloidal NPs. Faster cooling of the plasma leads to the production of more particles. In a colloid produced by PLA in a liquid, the higher the number of particles resulting from condensation, the smaller their average size [42]. Specific heat capacity and thermal conductivity are among the parameters affecting the cooling rate. In liquids with lower specific heat capacity and thermal conductivity, the cooling of the plasma plume is slower, resulting in the formation of larger NPs [39]. The lower specific heat capacity and thermal conductivity of acetone compared to water and ethanol is another reason for forming larger NPs in the acetone solution (Table 1 and Figures 6 and 7).

On the other hand, in the PLA process in liquid, the lower the density, viscosity, and surface tension of the liquid used, the weaker the plasma plume confinement conditions appear, leading to the formation of a larger plasma plume, resulting in larger NPs [36, 39, 43]. The viscosity of acetone is significantly less than water and ethanol, which could be another decisive reason for forming larger NPs in acetone solution. According to the above, the formation of larger NPs in acetone solution than other liquids used in the ablation process is due to the higher transmittance and smaller viscosity, density, specific heat capacity, and thermal conductivity of acetone.

Compared to ethanol and acetone, pure water has the lowest transmittance at 1064nm wavelength and the highest surface tension, density, boiling point, specific heat capacity, and thermal conductivity. Firstly, the smaller transmittance is, the less energy reaches the target surface. Secondly, higher surface tension and density create stronger plasma plume confinement

**Table 1.** Physical and chemical properties of materials of ablation environments[19-21].

Material	Pure Water	Pure Ethanol	Pure Acetone	CTAB
<b>Chemical formula</b>	H <sub>2</sub> O	CH <sub>3</sub> -CH <sub>2</sub> -OH	CH <sub>3</sub> -CO-CH <sub>3</sub>	C <sub>19</sub> H <sub>42</sub> BrN
<b>Chemical structure</b>				
<b>Boiling point(°C)</b>	100	78.37	56.3	-
<b>Specific heat capacity(J/gK)</b>	4.184	2.430	2.14	-
<b>Density(g/cm<sup>3</sup>)</b>	0.998	0.789	0.79	-
<b>Viscosity(cP)</b>	0.982	1.209	0.316	-
<b>Dipole moment(D)</b>	1.85	1.69	2.191	-
<b>PH</b>	7	7.33	7	-
<b>Dielectric constant</b>	78.4	25.3	20.7	-
<b>Refractive index at the wavelength of 1064 nm</b>	1.3204	1.36371	1.36135	1.44
<b>Optical transmittance along 1cm in the liquid</b>	0.54559	≈1	≈1	-
<b>Thermal conductivity (W/m.K)</b>	0.595	0.167	0.161	-
<b>Surface tension (mN/m)</b>	71.86	22.39	25.20	-

conditions. Thirdly, higher boiling point, specific heat capacity, and thermal conductivity cause faster cooling of the plasma plume and cavitation bubbles. Both the reaching less energy to the target surface and stronger confinement make the formation of a smaller plasma plume. Finally, forming a smaller plasma plume and faster cooling of it leads to the production of NPs with the smallest average size in distilled water.

The formation of larger NPs in the aqueous CTAB solution than distilled water can be attributed to the reduction of surface tension due to the addition of CTAB surfactant. In fact, by adding CTAB surfactant to the water environment, micelles are formed and reduce the surface tension of water [15,16].

### 3.6 UV–Vis–NIR absorption spectra

The absorption spectra of colloidal solutions prepared in different liquid environments were recorded using a UV–vis–NIR spectrometer in the wavelength range of 200–1100 nm with respect to the corresponding liquid absorbance as the baseline using quartz cells of 1cm × 1cm. In Figure 9, these spectra are shown in the wavelength range of 200–500 nm because they did not represent specific information at wavelengths higher than 500 nm. The observed absorption peaks can be due to the exciton absorption of WO<sub>3</sub> NPs or the surface plasmon absorption of W NPs [44–46].

The spectra show that the absorption starts at around 400 nm and increases towards shorter wavelengths. This property conforms to the reported absorption characteristics for WO<sub>3</sub>. In each spectrum, with decreasing wavelength, we observe one shoulder and one or two peaks. The positions of the shoulders and peaks observed in spectra of samples prepared in different liquid environments are given in Table 2. The shoulder position matches the exciton absorption peak position of WO<sub>3</sub> [37,44]. Since the surface plasmon resonance absorption of the W occurs in the UV spectral region [47], we believe that the peaks observed in the UV–vis spectra originate from the surface plasmon resonance absorption of the W. Also, the existence of both the W and the WO<sub>3</sub> was confirmed by the XRD spectra. In the spectra, plasmon and exciton absorption peaks of W and WO<sub>3</sub> have overlapped together; since the exciton absorption is weaker than plasmon absorption has appeared as a shoulder.

In the spectra of samples 1 and 4, two plasmon absorption peaks are observed. One possible explanation for this double peak could be related to the coarseness of some particles due to their aggregation in the two environments [47]. According to particle size distribution histograms, the double peak in sample 4 can be attributed to the formation of a significant number of particles larger than 100 nm. In sample 1, the

**Table 2.** Introduction of samples, the size distribution of NPs (taken from TEM images,) and plasmon/exciton resonance wavelengths of W and WO<sub>3</sub> NPs (taken from UV–Vis–NIR spectra) in different environments.

Liquid Environment	Water	Ethanol	Acetone	CTAB
Sample	1	2	3	4
Average size (nm)	49.54	66.27	79.24	71.07
Standard deviation (nm)	27.19	26.67	32.39	35.52
Plasmonic resonance wavelength (nm)	219,231	216	234	212,231
Excitonic resonance wavelength (nm)	262	279	278	275

number of particles larger than 100 nm is not significant, so the coarseness of some particles can not be a decisive reason for the duality of the peak in the spectrum of this sample. One of the other factors affecting the number of plasmonic peaks in the absorption spectra is the shape of the nanostructures. For spherical particles, a single adsorption peak appears in the adsorption spectra [6], and when the nanostructures shape changes from the sphere to the rod, a single plasmon peak splits into two peaks [48]. In the FESEM and TEM images of our samples, rod-shaped nanostructures are not observed. Hence it is reasonable to assume that the cause of the duality of the peaks because of their nearness to each other is the quasi-sphericity of NPs. In sample 1, the quasi-sphericity of NPs is more noticeable, which causes two plasmon peaks close to each other in the absorption spectrum. In samples 2 and 3, a single plasmon peak is seen because, in these samples, NPs are spherical, and the coarseness of some particles is not noticeable.

The dependence of optical absorption spectra on characteristics of NPs such as size, size distribution, shape, and material causes UV–vis spectroscopy to be an appropriate approach for investigating the optical properties of NPs. The size of semiconductor NPs affects their electronic structure. With decreasing the size of NPs, the bandgap energy increases. Absorption spectra present a qualitative study of the size and size distribution of NPs. In the absorption spectrum of colloidal NPs, with increasing the size of NPs, the absorption peak is shifted to a larger wavelength and vice versa. In other words, increasing the size of NPs in the samples causes a redshift in the absorption spectrum. The full width at half maximum (FWHM) of the excitonic absorption peak of semiconductor NPs depends directly on the width of the size distribution curve of NPs [5,27].

On the other hand, according to Mie scattering theory for small particles, the position and number of plasmonic absorption peaks and the shape of the spectra depend on the size, shape, and material of NPs and the dielectric function of the environment surrounding them. Absorption broadening depends on the size distribution and aggregation of NPs. Mie theory shows that increasing the size of NPs causes the redshift of the plasmon absorption peak and the decrease in the FWHM of the plasmon absorption and vice versa [2,6,48–51].

On the one hand, the existence of various factors affecting the shape, position, width, and number of peaks, and on the other hand, the overlap of excitonic and plasmonic peaks has complicated the analysis of spectra. Therefore, the accurate comparison of spectrum characteristics using our data is difficult. Despite this, the following results can be extracted from the spectra. As mentioned earlier, the exciton and the plasmon peaks shift toward larger wavelengths when the average nanoparticle size increases. Therefore, in Figure 9, the redshift of the absorption peak of sample 3 relative to the other samples can be attributed to forming NPs with the maximum average size in this environment. That part of the absorption peak that can be attributed to the plasmonic resonance effects and be independent of the exciton resonance effects is narrower in sample 3. Because according to Mie theory, the larger the average nanoparticle size is, the narrower FWHM of the peak is.

### 3.7 PL spectra

The photoluminescence (PL) spectroscopy is an advantageous method to identify the existence of different types of defects, oxygen vacancies, and lattice distortions in metal oxides [52,53]. The PL emission spectra of the samples prepared in the different liquid environments are depicted in Figure 11. The PL spectra have been recorded at room temperature under 200 nm excitation wavelength.

Figure 11 shows the UV–vis emissions centered at 295 and 300 nm in sample 1 and 295 nm in sample 4. We guess that UV–vis emissions are due to the localized state of oxygen vacancies in WO<sub>3</sub>. Karazhanov et al. applied first-principles pseudopotential calculations and proposed that oxygen vacancies in WO<sub>3</sub> are related to three types of defect states: 1) donor-like state within the fundamental bandgap, 2) hyper deep resonant state in the valence band, and 3) high-lying resonant state in the conduction band [54]. Therefore, the UV–vis emissions observed in the spectra of samples 1 and 4 are due to the localized state of oxygen vacancies corresponding to the high-lying defect state in the conduction band of WO<sub>3</sub> NPs. The intensity of UV–vis emission in sample 4 is lower than in sample 1, which may indicate a decrease in oxygen vacancies or a decrease in the number of WO<sub>3</sub> NPs produced in CTAB solution in comparison with distilled water. The

spectra of samples 2 and 3 present no UV–vis emission. It indicates the absence of the localized state of oxygen vacancies corresponding to the high-lying defect state in the conduction band of WO<sub>3</sub> NPs.

The PL spectra illustrate four peaks centered at about 423, 436, 446, and 472 nm attributed to the blue emissions of WO<sub>3</sub> NPs. The peak observed at 423 nm wavelength has maximum intensity. On the other hand, the blue emission of bulk phase WO<sub>3</sub> powder with maximum intensity has been reported at the wavelength of 467 nm [55,56]. Thus, the blue emissions of the WO<sub>3</sub> NPs produced by us have a blue shift relative to the blue emissions of the WO<sub>3</sub> bulk phase. According to matching the photon energy of 423 nm (2.93 eV) with bandgap energy reported in reference [52] for WO<sub>3</sub> NPs, and observing blue emissions in the spectrum of all samples, it is reasonable to suggest that the blue emissions are due to band to band transitions[55,56]. Investigating the PL spectra does not show a clear relationship between the size of NPs produced in different liquid environments with blue emissions. It means that the effect of quantum confinement on the bandgap is weak in our experiment [57].

The green emission peak found at 528 nm have occurred due to surface defects in WO<sub>3</sub> NPs [52,53]. Other researchers have also reported similar UV–vis, blue, and green emissions in the PL spectra of WO<sub>3</sub> nanostructures [52, 53, 55, 56].

#### 4. Conclusion

PLA of a pure W target was performed in distilled water, ethanol, acetone, and CTAB solutions. XRD patterns, FTIR spectra, and TEM images showed the formation of W-WO<sub>3</sub> composite NPs in all samples. The shape of NPs produced in all environments was spherical or nearly spherical. NPs produced in the distilled water, ethanol, and CTAB solutions were strongly adhesive that can be related to the hydrogen bond due to the OH functional group between NPs and molecules of water or ethanol. Due to the high dipole moment of the acetone molecules and the formation of electrical double layers around NPs in the acetone solution, no adhesion was observed between the prepared NPs in this solution.

The liquid characteristics such as refractive index, density, viscosity, surface tension, specific heat capacity, boiling point, and thermal conductivity control the size of produced NPs by affecting the cooling rate and confinement of the plasma plume. In the sample prepared in acetone solution, NPs had the largest average size and standard deviation. It is due to the higher transmittance and smaller viscosity, density, specific heat capacity, and thermal conductivity of acetone. NPs produced in distilled water had the smallest average size because compared to ethanol and acetone, pure water has lower transmittance and higher surface tension, density, boiling point, specific heat capacity, and thermal conductivity, causing the formation of a smaller plasma plume and faster cooling rate. On the other hand, adding CTAB surfactant to distilled water caused increasing the average size of NPs and decreasing their adhesion by reducing surface tension and creating a micelle

layer around the NPs, respectively.

The results of the UV–vis spectra also presented the exciton and plasmon resonance absorption of W and WO<sub>3</sub> NPs in all samples. In the spectra of samples prepared in distilled water and CTAB solution, two plasmon absorption peaks are observed relating to the coarseness of some NPs or the quasi-spherical of NPs. The PL spectra of all samples illustrate the green emission peaks due to surface defects and the blue emission peaks due to band-to-band transitions in WO<sub>3</sub> NPs. The UV–vis emissions observed in the spectra of samples prepared in distilled water and CTAB solution are due to the localized state of oxygen vacancies corresponding to the high-lying defect state in the conduction band of WO<sub>3</sub> NPs.

#### Conflict of interest statement:

The authors declare that they have no conflict of interest.

#### References

- [1] X. Zhao, Q. Di, M. Li, Q. Yang, Z. Zhang, X. Guo, X. Fan, K. Deng, W. Chen, and J. Zhang. *Chemistry of Materials*, **31**:4325, 2019.
- [2] R. Tilaki and S. Mahdavi. *Applied Physics A*, **84**:215, 2006.
- [3] H. Zheng, J.Z. Ou, M.S. Strano, R.B. Kaner, A. Mitchell, and K. Kalantar-zadeh. *Advanced Functional Materials*, **21**:2175, 2011.
- [4] F. Stokker-Cheregi, T. Acsente, I. Enculescu, C. Grisolia, and G. Dinescu. *Digest Journal of Nanomaterials and Biostructures (DJNB)*, **7**, 2012.
- [5] E. Solati, Z. Aghazadeh, and D. Dorrnian. *Journal of Cluster Science*, **31**:961, 2020.
- [6] R. Tilakia and S. Mahdavi. *Applied Physics A*, **88**:415, 2007.
- [7] F. Barreca, N. Acacia, E. Barletta, D. Spadaro, and F. Neri G. Curro. *Applied Surface Science*, **256**:6408, 2010.
- [8] M. Khademian, M. Zandia, M. Amirhoseiny, and D. Dorrnian. *Journal of Cluster Science*, **28**:2753, 2017.
- [9] G. Bajaj and R. Soni. *Applied Physics A*, **97**:481, 2009.
- [10] J. Zhang, J. Claverie, M. Chaker, and D. Ma. *ChemPhysChem*, **18**:986, 2017.
- [11] M.H. Mahdih and B. Fattahi. *Applied Surface Science*, **329**:47, 2015.
- [12] G. Wypych. *Handbook of solvents*. ChemTec, 1th edition, 2001.
- [13] E.M. Gonçalves and M.E.M. da Piedade. *Journal of Chemical Thermodynamics*, **47**:362, 2012.
- [14] C.Y. Ng, K.A. Razak, A.A. Aziz, and Z. Lockman. *Journal of Experimental Nanoscience*, **9**:9, 2014.

- [15] S. Das, S. Mondala, and S. Ghosh. *Journal of Chemical and Engineering Data*, **58**:2586, 2013.
- [16] M.J. Lehman. *embry riddle scholarly commons*, , 2016.
- [17] D. Joseph, R.D. Rodriguez, A. Verma, E. Pousaneh, H. Lang D.R. Zahn, and S. Chandra. *RSC advances*, **7**:3628, 2017.
- [18] B. Bagchi. *Water in biological and chemical processes: from structure and dynamics to function*. Cambridge University Press, 2th edition, 2013.
- [19] D. Lide, W. Haynes, G. Baysinger, L. Berger, and M. Frenkela nd R. Goldberg. *CRC Handbook of Chemistry and Physics*. CRC Press/Taylor and Francis, 90th edition, 2010.
- [20] J. Rheims, J. K"ösera, and T. Wriedt. *Measurement Science and Technology*, **8**:601, 1997.
- [21] G.M. Hale and M.R. Query. *Applied optics*, **12**:555, 1973.
- [22] M. Ranjbar, A.H. Fini, H. Kalhori, P. Kameli, and H. Salamat. *Solar Energy Materials and Solar Cells*, **132**:329, 2015.
- [23] C.M. Wu, S. Naseem, M.H. Chou, J.H. Wang, and Y.Q. Jian. *Frontiers in Materials*, **6**:49, 2019.
- [24] P. Kazakevich, A. Simakin, V. Voronov, and G.A. Shafeev. *Applied Surface Science*, **252**:4373, 2006.
- [25] Y. Wang, X. Su, and S. Lu. *Journal of Materials Chemistry*, **22**:1969, 2012.
- [26] A.V. Kadam and S.B. Patil. *Materials Research Express*, **5**:085036, 2018.
- [27] M. Moradi, E. Solati, S. Darvishi, and D. Dorrnian. *Journal of Cluster Science*, **27**:127, 2016.
- [28] H. Zeng, W. Cai, Y. Li, J. Hu, and P. Liu. *Journal of Physical Chemistry B*, **109**:18260, 2005.
- [29] P.J. Boruah, R.R. Khanikar, and H. Bailung. *Plasma Chemistry and Plasma Processing*, **40**, 2020.
- [30] M. Daniel, B. Desbat, J. Lassegues, B. Geranda, and M. Figlarz. *Journal of solid state chemistry*, **67**:235, 1987.
- [31] S. Shukla, S. Chaudhary, A. Umar, G.R. Chaudhary, and S. Mehta. *Sensors and Actuators B: Chemical*, **196**:231, 2014.
- [32] A.B. Habtemariam and Y. Alemu. *Biointerface Research in Applied Chemistry*, **12**:529, 2022.
- [33] E.I. Ross-Medgaarden and I.E. Wachs. *Journal of Physical Chemistry C*, **111**:15089, 2007.
- [34] H.F. Pang, X. Xiang, Z.J. Li, Y.Q. Fu, and X.T. Zu. *Physica Status Solidi (a)*, **209**:537, 2012.
- [35] K.A. Abdullin, Z.K. Kalkozova, A.A. Markhabayeva, R. Dupre, M. Moniruddin, and N. Nuraje. *ACS Applied Energy Materials*, **2**:797, 2018.
- [36] V. Amendola and M. Meneghetti. *Physical Chemistry Chemical Physics*, **21**:3027, 2013.
- [37] A.K. Deb, P. Chatterjee, and S.P. SenGupta. *Actamater*, **52**:2755, 2004.
- [38] F. Alizadeh S.A. Rashid A.R. Sadrolhosseini, M.A. Mahdi. *Laser Technology and its Applications*. IntechOpen, 1th edition, 2018.
- [39] S.C. Singh, H. Zeng, C. Guo, and W. Cai. *Nanomaterials: processing and characterization with lasers*. John Wiley and Sons, 1th edition, 2012.
- [40] M. Kosmulski. *Surface charging and points of zero charge*. CRC press, 1th edition, 2009.
- [41] K. Choudhury, R.K. Singh, P. Kumar, M. Ranjan, A. Srivastava, and A. Kumar. *arXiv Plasma Physics*, **2**, 2018.
- [42] G. Yang. *Laser Ablation in Liquids: Principles and Applications in the Preparation of Nanomaterials*. CRC Press, 1th edition, 2012.
- [43] E. Fazio, B. G"ökce, A. De Giacomo, M. Meneghetti, G. Compagnini, M. Tommasini, F. Waag, A. Lucotti, C.G. Zanchi, and P.M. Ossi. *Nanomaterials*, **10**:2317, 2020.
- [44] F. Barreca, N. Acacia, S. Spadaro, G. Curro, and F. Neri. *Materials Chemistry and Physics*, **127**:197, 2011.
- [45] A.M. Mostafa, S.A. Yousef, W.H. Eisa, M.A. Ewaida, and E.A. Al-Ashkar. *Journal of Molecular Structure*, **1185**:351, 2019.
- [46] O. Yayapao, T. Thongtem, A. Phuruangrat, and S. Thongtem. *Journal of Alloys and Compounds*, **509**:2294, 2011.
- [47] M. Lima, F. Ladario, and R. Riva. *Applied surface science*, **252**:4420, 2006.
- [48] J. Boken, P. Khurana, S. Thataia, D. Kumar, and S. Prasad. *Applied Spectroscopy Reviews*, **52**:774, 2017.
- [49] E. Solati and D. Dorrnian. *Journal of Cluster Science*, **26**:727, 2015.
- [50] O.A. Balitskii, D. Moszyński, and Z. Abbas. *RSC advances*, **6**:59050, 2016.
- [51] R. Tilaki and S. Mahdavi. *Journal of Nanoparticle Research*, **9**:853, 2007.
- [52] J. Kaur, K. Anand, A. Kaur, and R.C. Singh. *Sensors and Actuators B: Chemical*, **258**:10222, 2018.
- [53] T. Thilagavathi and D. Venugopal. *International Journal of Scientific Research and Reviews*, **7**:680, 2018.
- [54] S.Z. Karazhanov, Y. Zhang, A. Mascarenhas, S. Deb, and L.-W. Wang. *Solid State Ionics*, **165**:43, 2003.
- [55] J.Y. Luo, F.L. Zhao, L. Gong, H.J. Chen, J. Zhou, Z.L. Li, S.Z. Deng, and N.S. Xu. *Applied Physics Letters*, **91**:093124, 2007.

- [56] C. Veenas, L. Asitha, V.C. Bose, A.A. Raj, G. Madhu, and V. Biju. *Studies on the uv-visible and photoluminescent emission in nanocrystalline tungsten oxide*. IOP Publishing, 1th edition, 2015.
- [57] K. Lee, W.S. Seo, and J.T. Park. *Journal of the American Chemical Society*, **125**:3408, 2003.